A Multiscale Model for the Simulation of Sediment Impact Erosion of Metallic Targets using the Finite Volume Particle Method

Sebastián Leguizamón[1,*], Ebrahim Jahanbakhsh[1,2], Audrey Maertens[1], Siamak Alimirzazadeh[1], François Avellan[1]
[1]Laboratory for Hydraulic Machines, École Polytechnique Fédérale de Lausanne (EPFL), Lausanne, Switzerland
[2]Institute of Computational Science, Università della Svizzera Italiana, Lugano, Switzerland
[*]sebastian.legui@epfl.ch

***Abstract*—Erosion damage in hydraulic turbines is a common problem caused by the impact of sediments entrained in the fluid. Simulating this erosion process is very challenging because of the wide range of time and space scales involved. Conforming to the nature of the problem, a novel multiscale model of erosion is presented in this paper. Two different scales are simulated: a microscopic scale resolving the sediment impacts and the local material erosion, and a macroscopic scale accounting for the sediment transport and the global erosion distribution. A communication strategy between these scales allows reproducing the original coupled problem, enabling the simulation of the erosion process of a real-world component without relying on erosion correlations. The slurry jet erosion case is chosen for validating the proposed model. The global erosion rate and the local erosion depth are compared against their experimental counterparts, showing good agreement.**

I. Introduction

Hydroabrasive erosion is a complex phenomenon which consists in the gradual removal of material from a surface in contact with a sediment-laden flow. Hydraulic machines, as well as several other industrial components, are subject to hydroabrasive erosion, which results in efficiency degradation, cavitation enhancement, increased vibration and outage for expensive repairs [1]. This erosion damage can be diminished by a combination of design, operation and maintenance choices, *e.g.* surface coatings, ad hoc turbine geometry, strategic shutdown in periods of high sediment concentration, periodic welding repairs, etc; any such choice yields some reduction in damage at a given economic cost. The ability to predict the erosion damage a turbine under specific conditions will experience would prove invaluable in the aforementioned cost-reduction decision making.

The erosion damage of a given surface depends on a wide range of parameters [2]. Perhaps the most relevant ones are the angle and velocity at which sediments tend to impact the surface, as well as the size of the particles. These impact conditions depend on other factors such as the fluid and flow characteristics such as density, viscosity and turbulence. Moreover, the damage induced by these impact conditions is very sensitive to the surface material properties, as well as the sediment shape and hardness.

Six decades of experimental investigations have provided important insight into the mechanisms driving this complex phenomenon. Finnie [3]–[5] investigated the erosion characteristics of ductile and brittle materials and proposed simple analytical models to predict the amount of mass removed by any given impact. Bitter [6], [7] proposed another analytical model based on studies of two erosion mechanisms on ductile materials: the accumulation of plastic deformation, predominant at high impact angles, and the removal of material by cutting, effective at low impact angles. Both of these models are still used to date on a variety of empirical erosion correlations [2]. Shewmon [8] highlighted the importance of the rate of strain and thermal effects, as well as the formation of lips and craters on the surface of the metal which play an important role in subsequent impacts. In spite of these insights, experimental investigations under laboratory conditions are seldom transposable to real conditions because of the lack of dynamic similarity between model and prototype [2], which cannot be achieved due to the large number of parameters involved in the erosion phenomenon. Similarly, the available erosion correlations lack generality and predictive power [9], undermining their applicability.

Numerical simulations have been used to study the erosion phenomenon following two very different approaches. On the one hand, the microscopic details of high strain-rate solid particle impacts have been studied with both the finite element method [10]–[12] and smoothed particle hydrodynamics [13]–[15]. Even though the sophisticated constitutive modeling used in this approach allows capturing the thermomechanical behavior of the impacted surface, it is only applicable to microscopic domains due to its high computational cost. In other words, this approach provides the great advantage of calculating the erosion based on the physical behavior of the material, yet it is not applicable to real-world erosion problems. On the other hand, the second approach that has been used to model hydroabrasive erosion relies on tracking the sediment particles using computational fluid dynamics [16]–[18]. Although applicable to large, real-world erosion problems, this approach lacks the microscopic resolution to model the sediment impacts. It therefore has to fall back on

erosion correlations to close the system, *i.e.* determine the amount of material removed by any given impact, as well as the sediment rebound velocity. Even though it is possible to find a correlation that can be tunned to any particular data set, it has been found that such tunned correlations perform very poorly on any other data set [9], as expected. Accordingly, the predictive power of this approach is very limited.

In this paper, a novel multiscale model of erosion is presented which takes advantage of the benefits of the aforementioned approaches. It enables simulating the erosion of a macroscopic domain whilst relying on microscopic simulations to calculate the impact-induced erosion. In Section II we present the mathematical models used, as well as the proposed multiscale strategy. Section III details the experimental validation of the model results. We draw a short discussion and conclusion in Section IV.

II. Modeling

A. Governing equations

The mass, linear momentum and energy conservation equations are solved for the three phases modeled: solid, fluid and sediment. They are expressed as

$$\frac{d\rho}{dt} + \rho\nabla\cdot\boldsymbol{C} = 0 \tag{1}$$

$$\rho\frac{d\boldsymbol{C}}{dt} = \nabla\cdot(\boldsymbol{s} - p\boldsymbol{I}) + \boldsymbol{f} \tag{2}$$

$$\rho c_p\frac{\partial T}{\partial t} = \kappa\nabla^2 T + \dot{q} \tag{3}$$

where ρ is the density, $\boldsymbol{C}$ is the velocity, p is the pressure, T is the temperature, $\boldsymbol{s}$ is the deviatoric stress tensor, $\boldsymbol{f}$ is the sum of volumetric and surface forces, $\dot{q}$ is the sum of heat sinks and sources, and $\frac{d}{dt}$ denotes the material derivative. Constant heat capacity c_p and thermal conductivity κ are assumed in (3) when dealing with the solid, whereas the fluid and the sediments are both assumed isothermal.

1) Fluid constitutive model: The fluid is assumed Newtonian and weakly compressible; its pressure is therefore obtained from an equation of state. The following form of the Tait equation is usually considered for water [19]

$$p = \frac{\rho_\circ a^2}{\gamma}\left(\left(\frac{\rho}{\rho_\circ}\right)^\gamma - 1\right) \tag{4}$$

where $\rho_\circ$ is the reference density, a is the speed of sound and γ is set to 7. For a Newtonian fluid, using Boussinesq's eddy viscosity assumption, it follows that

$$\boldsymbol{s} = 2(\mu + \mu_t)\left(\dot{\boldsymbol{\varepsilon}} - \frac{1}{3}\mathrm{tr}(\dot{\boldsymbol{\varepsilon}})\boldsymbol{I}\right) - \frac{2}{3}\rho k\boldsymbol{I} \tag{5}$$

where μ is the dynamic viscosity, μ_t is the turbulence viscosity, k is the turbulence kinetic energy and $\dot{\boldsymbol{\varepsilon}}$ is the strain rate tensor, given by

$$\dot{\boldsymbol{\varepsilon}} = \frac{1}{2}\left(\nabla\boldsymbol{C} + (\nabla\boldsymbol{C})^T\right). \tag{6}$$

The standard k-ϵ turbulence model with the standard wall function is used to calculate the turbulence viscosity. Although relatively simple, this model has been shown to provide the same sediment flux prediction for a variety of impinging jet erosion test cases, compared to the low-Reynolds number k-ω SST model [9].

2) Sediment transport model: The sediment particles are modeled as rigid; their mass and volume are constant, therefore (2) reduces to Newton's second law:

$$m\frac{d\boldsymbol{C}}{dt} = m\boldsymbol{g} + \boldsymbol{f}_s + \boldsymbol{f}_f + \boldsymbol{f}_h \tag{7}$$

where m is the sediment particle mass. The sediment-solid contact force, $\boldsymbol{f}_s$, is calculated using a penalty method based on Hertz's contact theory, whereas the friction force, $\boldsymbol{f}_f$, is obtained from a static-kinetic Coulomb model.

The hydrodynamic force felt by the sediments, $\boldsymbol{f}_h$, takes into account several contributions. The most important one is the drag force, which is modeled using the drag coefficient correlation by Haider and Levenspiel [20] for non-spherical particles. The second most important hydrodynamic contribution is the force due to the fluid pressure gradient. Additionally, the effects of added mass, shear lift and buoyancy are also taken into account. For information concerning these formulations, the interested reader is referred to [21], [22].

In order to account for the effect of turbulence, we use the eddy interaction model by Gosman and Ioannides [23]. It assumes that each sediment interacts with a single eddy at a time, whose characteristic length, strength, and duration are calculated based on the local turbulence properties. The eddy induces a velocity fluctuation proportional to its strength, which affects the relative velocity between sediment and fluid, and therefore has an effect on the drag, added mass and lift forces.

We use a one-way coupling for the sediment transport: Only the fluid has an effect on the sediments. Neglecting the effect of the sediments on the fluid momentum is justified given the very low concentrations involved, which are commonly below 1% mass ratio.

3) Solid constitutive and damage models: The solid is modeled as homogeneous, isotropic and elasto-plastic. The linear stress-strain constitutive relation used in the elastic regime can we expressed as

$$\boldsymbol{\sigma} = \lambda_1\mathrm{tr}(\boldsymbol{\varepsilon})\boldsymbol{I} + 2\lambda_2\boldsymbol{\varepsilon} \tag{8}$$

where λ_i are Lamé's elasticity coefficients, $\boldsymbol{\varepsilon}$ is the elastic strain and $\boldsymbol{\sigma} = \boldsymbol{s} - p\boldsymbol{I}$ is Cauchy's stress tensor.

To calculate the pressure, the temperature-corrected Mie-Grünesen equation of state is used:

$$p = \rho_\circ a^2\mu_g\frac{1 + (1 - \frac{\gamma_\circ}{2})\mu_g}{\left[1 - (S-1)\mu_g\right]^2} + \gamma_\circ\rho_\circ c_p(T - T_\circ) \tag{9}$$

where $\mu_g = \frac{\rho}{\rho_\circ} - 1$, a is the bulk speed of sound, $T_\circ$ is the reference temperature, $\gamma_\circ$ is Grüneisen's parameter and S is the linear Hugoniot slope coefficient [24].

The radial return plasticity algorithm [25] is used together with the von Mises yield criterion to evolve the stress and induce the appropriate increases in plastic strain upon integration of the Jaumann rate of stress.

The Johnson-Cook [26] strength and damage models are used to calculate the yield stress and the failure plastic strain, respectively. They include the effects of nonlinear strain hardening, strain rate, thermal softening and triaxiality, and can be written as

$$\sigma_y = \left[A_1 + A_2 \varepsilon_p^n\right] \left[1 + A_3 \ln \frac{\dot{\varepsilon_p}}{\dot{\varepsilon}_\circ}\right] \left[1 - T_h^m\right] \tag{10}$$

$$\varepsilon_{p_f} = \left[D_1 + D_2 \exp\left(D_3 \frac{p}{\sigma_v}\right)\right] \left[1 + D_4 \ln \frac{\dot{\varepsilon_p}}{\dot{\varepsilon_\circ}}\right] \left[1 + D_5 T_h\right] \tag{11}$$

where A_i and D_i are material constants, ε_p is the equivalent plastic strain, n is the strain hardening exponent, $\dot{\varepsilon_p}$ is the plastic strain rate, $\dot{\varepsilon}_\circ$ is the reference strain rate, T_h is the homologous temperature and m is the thermal softening exponent.

The accumulation of plastic strain leads to material failure in ductile metals, in which case the affected particle is removed from the system. This occurs once the material damage, δ, reaches a value of 1.0. The cumulative damage law is written as

$$\delta = \sum_i \frac{\Delta\varepsilon_{p,i}}{\varepsilon_{p_f,i}} \tag{12}$$

where $\Delta\varepsilon_{p,i}$ is the plastic strain increment for time step i, and $\varepsilon_{p_f,i}$ is the failure plastic strain for time step i, according to (11).

Two heat sources are included within (3). The thermoplastic heating contribution is modeled as

$$\dot{q}_p = \beta \left(\boldsymbol{\sigma} : \dot{\boldsymbol{\varepsilon}}_p\right) \tag{13}$$

where β is the fraction of the plastic work converted to heat. The frictional contact contribution can be expressed as

$$\dot{q}_f = \eta \, \frac{\boldsymbol{f}_f \cdot \boldsymbol{C}_r}{A_f} \tag{14}$$

where η is the fraction of the friction heat transfered to the solid, $\boldsymbol{C}_r$ is the relative velocity between sediment and solid, and A_f is the contact area. The material properties determine η for each body according to the following expression [27]

$$\eta_1 = \left(1 + \sqrt{\frac{\kappa_2 c_{p_2} \rho_2}{\kappa_1 c_{p_1} \rho_1}}\right)^{-1} \tag{15}$$

where κ_i, c_{p_i} and ρ_i are the thermal conductivity, heat capacity and density of body i.

B. The finite volume particle method

The aforementioned models are discretized using the finite volume particle method (FVPM), which is a recently developed meshless method that takes advantage of many of the desirable features of conventional mesh-based finite volume methods, while maintaining the convenience of the particle-based approach.

FVPM is based on an arbitrary Lagrangian-Eulerian (ALE) formulation, providing computational nodes the flexibility to move with an arbitrary velocity. This flexibility implies a convenient advantage for handling moving interfaces. FVPM is therefore well suited for free surface flow problems as well as cases where significant deformations are expected, such as particle impact simulations where traditional mesh-based methods suffer from excessive mesh distortion and tangling [13], [14]. Unlike SPH, FVPM is both consistent and conservative [28]. Furthermore, it has recently been shown to provide higher accuracy compared to SPH, achieving second-order convergence [29].

FVPM can be understood as a generalization of the traditional finite volume method [30], with spherical volumes, *i.e.* particles, that are allowed to move and overlap. The flux exchange between volumes is weighted by interaction vectors, analogous to the area vectors defined on the surfaces of traditional finite volumes. These interaction vectors are integrated exactly by using sphere-supported top-hat kernel overlaps.

Inviscid and pressure fluxes are computed using AUSM$^+$, an approximate Riemann solver proposed by Liou [31] and extended by Luo et al. [32] for the ALE formulation. Time integration is performed with the second-order explicit Runge-Kutta scheme. For a detailed derivation of the 3D-FVPM formulation, the exact computation of interaction vectors using spherical-support kernels, several validation cases and applications, the reader is referred to [19], [28], [29], [33]–[35].

C. Multiscale modeling of the erosion process

Most phenomena in nature have a multiscale character, such that the observable macroscopic behavior emerges from countless microscopic interactions [36], [37]. The direct numerical simulation of all these interactions is oftentimes intractable for any problem of interest. Specific multiscale strategies have therefore been developed to tackle this type of problem, for instance [38]–[41]. The general denominator of this kind of strategy can be stated as: decouple the problem into a set of subproblems according to the characteristic scales present; formulate models suitable for the level of detail required in each subproblem; design a communication algorithm such that the results of the detailed microscale model are used to provide closure to the coarser macroscale model.

Not surprisingly, the particle impact erosion phenomenon is inherently multiscale. It is a gradual process over large-scale surfaces, yet it is caused by countless microscopic, ephemeral particle impacts. Its multiscale nature explains the difficulty in simulating this problem, as well as the two approaches that

have thus far been used: either the simulation of a handful of impacts on a microscopic domain, or the simulation of macroscopic correlation-based erosion. The novel multiscale model proposed uses the information provided by microscale impact simulations to provide closure to the macroscale erosion simulation, avoiding the use of uncertain correlations to estimate the amount of mass removed by any given impact.

By decoupling the sediment impact and transport processes, the computational intensity of the problem is significantly reduced. The restrictive time steps and fine discretization inherent to the solid model are only required for the microscale impact simulations, whereas the hydrodynamic transport simulation benefits from much longer time steps and coarser discretization, in line with its slow dynamics and large domain. The challenge lies in designing the communication necessary between scales in order to reproduce the original coupled problem. We opt for a sequential multiscale strategy whereby a set of microscale impact simulations is performed before launching the macroscale transport simulation. Although a concurrent multiscale approach is possible in principle, *e.g.* perform a microscale simulation every time an impact is detected in the macroscale simulation, the enormous number of impacts expected and number of microscale domains required renders this possibility unpractical. The details of each submodel are explained hereafter.

1) Microscale modeling: Solid particle impacts: Any given microscale simulation involves a solid material sample receiving a large number of sediment impacts at constant conditions, *e.g.* particle size, impact velocity and angle. The space of possible impact conditions is explored by performing a finite set of independent microscale simulations whose aggregated results serve as closure to the macroscale model. The information extracted from the simulations is two-fold: the average particle rebound velocity in the form of restitution coefficients, and the steady-state erosion rate at those particular impact conditions. The latter one is defined as the slope of the accumulated eroded mass *vs.* accumulated erodent mass curve, which only becomes linear after an initial incubation period within which plastic strain accumulates on the sample. Between 100 and 300 impacts are required before the solid starts to fail ($\delta > 1.0$) and the erosion curve reaches a steady-state slope.

Fig. 1 illustrates the computational domain for one of the microscale simulations used in the validation test case. Two simplifications are used in the proposed model. First, similar to [42], [43], we disregard the effect of the fluid within the microscale model, since the presence or absence of liquid at the instant of impact has a negligible effect for the impact results [44] at the high Stokes number of about 500 characteristic of sand sediments in water at typical transport velocities. This disregard for the effect of the fluid during the collision instant should not be confused with the significant effect the fluid has before it, which is captured by the macroscale model. Second, heat conduction in the solid is neglected such that the temperature only changes through the source terms $\dot{q}_i$. Indeed, the impact dynamics considered is so fast that the heat generated by the plastic deformation of the metal has no time to diffuse during the impact duration, leading to an adiabatic temperature increase [8], [42]. Unphysical heat accumulation during successive impacts is avoided by relaxing the temperature back to the reference level after each impact. By using this approach, the local temperature increase and its effect on the material response are considered, without the need to solve the conjugate heat transfer problem.

2) Macroscale modeling: Solid particle transport: The macroscale model is in charge of solving the turbulent sediment transport through the domain. The solid surface being eroded is discretized by a single layer of fixed particles which acts as a no-slip wall with respect to the fluid. These particles also serve as the bridge between scales: Each time a sediment contacts one of these particles, the set of microscale simulation results is interpolated based on the current impact conditions (velocity, angle, diameter) in order to define the outcome of the collision. That is, the restitution coefficients calculated from the detailed microscale simulations determine the fraction of the normal and tangential impact velocities that is conserved. Similarly, the steady-state erosion rate interpolated from microscale results, together with the impacting sediment mass, determine the amount of mass removed by the collision. Note that, unlike the solid particles in the microscale model, the macroscale wall particles are never eroded away; they only store a scalar value of removed mass.

As the simulation advances, the wall particles accumulate the information pertaining to each impact, providing probability density distributions of impact conditions, as well as erodent flux and total eroded mass, at each point on the surface. After a large number of sediments have been injected through the inlet boundary, one obtains a statistically-significant erosion distribution over the surface of interest.

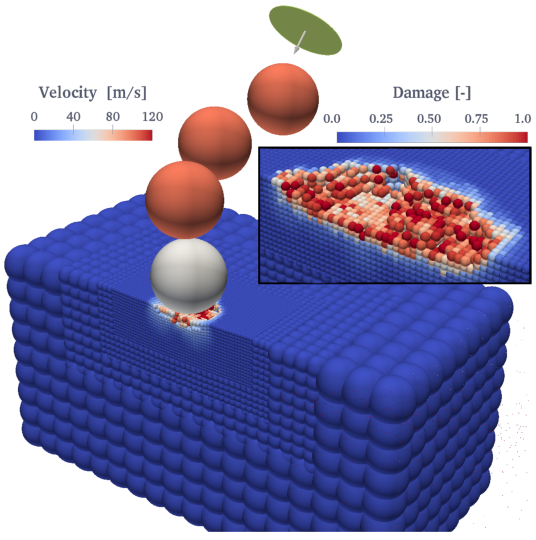

Fig. 1. Microscale model domain comprised of the inlet, impacting spherical sediments and the solid sample, which is only half-visible. A detailed view of the eroded zone after 150 impacts is also presented.

III. Model validation

A. Test case description

The slurry jet erosion of a flat plate is chosen as the validation test case because it includes all the aforementioned phenomena reduced to their simplest expression. We use the experimental data by Sugiyama, Harada and Hattori [16]. They conducted slurry erosion tests on oxygen-free copper JIS-C1020 at a jet velocity $C_\circ = 10$ ms^{-1} and impingement angle of $90°$. The jet nozzle, with a radius $r_\circ = 1.5$ mm, was set with a standoff distance of 25 mm. The slurry was prepared with water and silica sand to a concentration of 1% by weight. They performed profilometry of the erosion pattern as well as measuring the overall erosion rate.

The material properties and model parameters required to perform our simulations are taken from [24], [26], [45]. The macroscale domain comprises the 3 mm diameter slurry jet impinging on a 10 mm $\times$ 10 mm flat plate, as illustrated in Fig. 2. The standoff distance was set to 5 mm to save computational resources. This choice is justified because no discernible difference in the flow field was noticed above this distance, partly because no jet dispersion occurs since we do not model the air phase.

The sediment diameters are randomly drawn from a Weibull distribution according to the experimental data [16] and then randomly seeded on the inlet boundary with the same velocity as the fluid. The normal distance between successive sediment injections is chosen such that the experimental concentration is reproduced. Unlike common CFD particle tracking, our model does take into account inter-sediment collisions.

The experimental Reynolds number and the distribution pipe length suggest a fully developed turbulent flow at the inlet. Consequently, Nikuradse's [46] velocity and turbulence profiles for straight pipe flow are specified on that boundary.

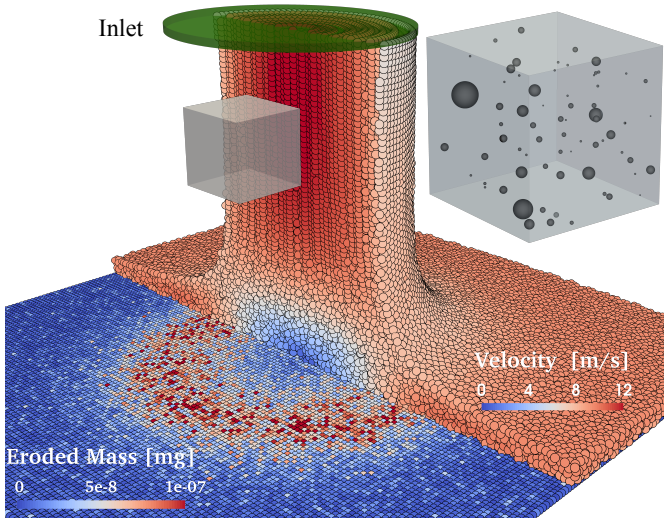

Fig. 2. Macroscale model comprised of the flat plate, the inlet and the impinging jet, which is only half-visible. The sediments within a 1 mm^3 box are rendered, whereas all the rest are excluded for the sake of clarity.

The microscale domain, presented in Fig. 1, comprises the copper sample and a circular inlet through which the sediments are injected. A parametric analysis has been performed to assess the dependence of the erosion rate results on the microscale simulation setup. Aspects such as the size of the area where the impacts are allowed to occur, the separation between successive impacts, the size of the domain and the level of discretization refinement are chosen to ensure that the results are independent of the setup. A resolution of 16 solid particles per sediment diameter is used. The microscale simulations are performed for the following impact angles: 30, 45, 60 and $90°$, and impact velocities: 50, 80, and 100 ms^{-1}. Such high velocities are necessary to estimate the erosion rate within a reasonable number of impacts (100 to 300 in this particular case) due to the constraints to computational time; these results are then extrapolated to the lower impact velocities occurring in the test case.

A convergence analysis of the sediment impact condition distributions in terms of the fluid resolution suggests an independent result with 32 fluid particles per jet diameter. It was also found that the required amount of sediments to achieve converged distributions of the variables of interest on the surface was about $3\text{x}10^5$.

B. Validation Results

Given the axisymmetry of the problem, the results are azimuthally-averaged to allow for a quantitative chart representation. Fig. 3 depicts the sediment flux as a function of radial position, both across the inlet boundary and against the copper surface. Note that the integral of these two curves needs not be equal since not every sediment entering the domain impacts the surface once; some impact it more than once while others never impact.

It is clear that the highest sediment flux against the surface occurs below the jet inlet, where the sediments struggle to follow the highly curved fluid streamlines. This inertia-driven process is dependent on the sediment diameter, with smaller particles following the fluid more closely. This explains why the average diameter of impacting particles, also shown in Fig. 3, is greater below the inlet. Note that the sediment flux does not vanish even when the mean fluid velocity is parallel to the surface ($r/r_\circ >\sim 2.0$) because of the effect of turbulence. As expected, such turbulent velocity fluctuations have a greater effect on low-inertia particles, as evidenced by the decreasing average diameter with increasing radial position trend.

The sediment flux is not the best predictor of erosion; it is all about the impact conditions, rather than the bare number of impacts. Fig. 4 depicts the average impact angle and velocity as a function of distance from the jet center. Note that the standard deviation, depicted by the error bars, represents the average impact condition variability at a given radial position; it is calculated as the azimuthal average of the standard deviation stored in each wall particle, itself a function of the impacts which that particle registered. In other words, the depicted standard deviation is not a measure of azimuthal variability, which is almost nonexistent.

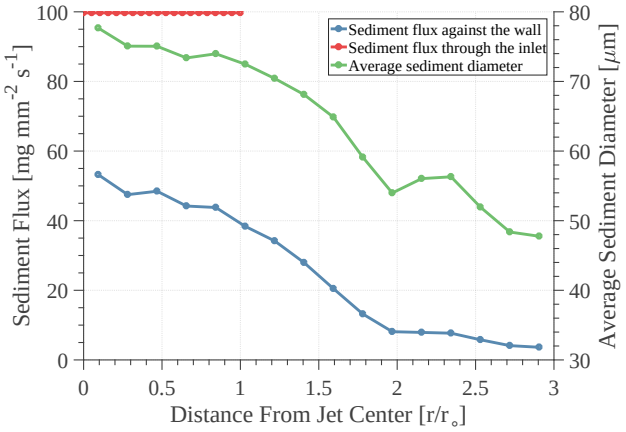

Fig. 3. Sediment flux through the inlet and against the copper surface, and average diameter of impacting particles as functions of the distance to the jet center normalized by the jet radius $r_\circ$.

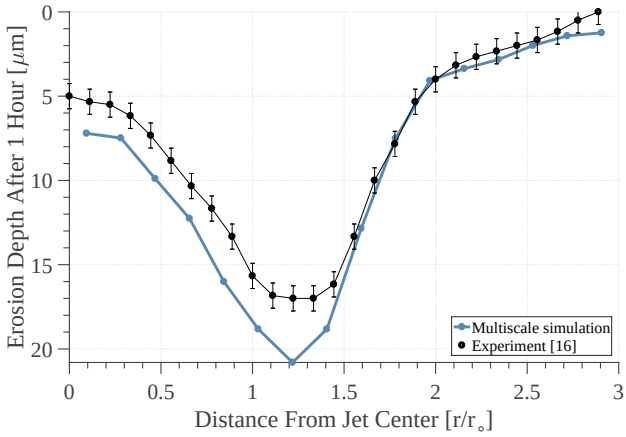

Fig. 5. Comparison of experimental [16] and numerical eroded depth profiles after one hour. The experimental error bars represent the average standard deviation of averaging two coplanar profilometry measurements.

The particle transport behavior presented in Fig. 4 is the following: The area underneath the jet inlet is characterized by low-velocity impacts at normal incidence, due to the low-velocity stagnation region and the jet orientation, respectively. Conversely, the particles which follow the fluid streamlines to a greater extend end up impacting at higher velocity and lower impact angle further downstream.

Note that the impact condition which a specific particle will be subject to does not only depend on its size, but also on its initial position on the inlet boundary and on turbulence-induced randomness. These circumstances explain the relatively high standard deviation in both impact velocity and angle.

The interaction of the microscale erosion model results and the distributions of impact conditions and erodent flux gives rise to the eroded mass profile presented in Fig. 5. As further discussed in Section IV, the eroded mass after the short simulation time is extrapolated to calculate the eroded mass after one hour, therefore allowing the comparison with the experimental profilometry data.

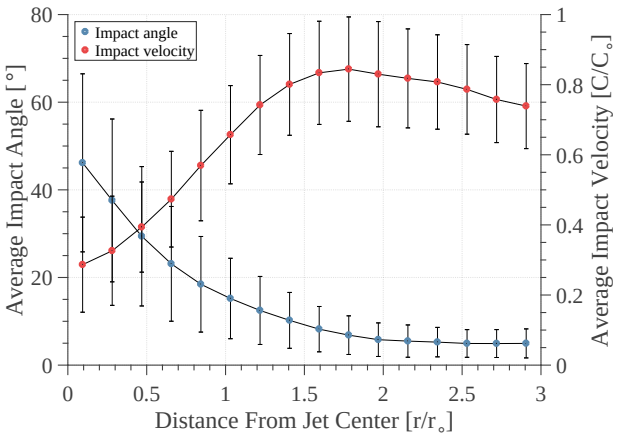

Fig. 4. Average impact angle and velocity as functions of the distance to the jet center. The impact velocity is normalized by the jet velocity $C_\circ$, whereas the distance is normalized by the jet radius $r_\circ$. The error bars represent $\pm$ one standard deviation.

Fig. 5 evidences a good agreement between the experimental data and the simulation results. Furthermore, the global erosion rate also compares well: 3.42 mg kg^{-1}, a 16% difference with respect to the value of 2.95 mg kg^{-1} reported in the experiment. These results are very encouraging and serve as initial validation of the proposed multiscale erosion model.

IV. Discussion and Conclusion

As illustrated in Fig. 5, the predicted eroded depth does not vanish near $r/r_\circ = 3$, in disagreement with the experiment. This implies that if a larger domain were to be simulated, the global erosion rate would be further overpredicted. This mismatch is perhaps due to an overprediction of turbulence intensity in the thin liquid film resulting from the impinging jet divergence. Local refinement would be required to better capture the velocity and turbulence profiles in this thin film; only a handful of particle do so in the presented results.

The assumption of constant erosion rate implicit in the choice of extrapolating the results of a short macroscale simulation to compare with an hour-long experiment may be challenged on the grounds of the erosion delay due to the incubation period, or on the effect of the surface alteration on the erosion rate. The former objection is not relevant, since the erosion incubation period is accounted for in the microscale simulations; even if the macroscale simulations are short, they do represent the long-term erosion behavior in virtue of the steady-state erosion rate they use, calculated from the long microscale simulations. The latter objection is not justified for this particular case, since the surface modification (erosion depth corresponding to about 0.3% of the jet diameter after one hour) should not induce any significant change in the sediment transport hydrodynamics. We acknowledge that, for cases where the surface modification becomes significant, the altered hydrodynamics may lead to a modified erosion

rate distribution, in which case the extrapolation from a short macroscale simulation would induce additional error.

In this paper, we have presented a novel multiscale model for the simulation of sediment impact erosion. Conforming to the multiscale nature of the phenomenon, we simulate two different scales which account for the sediment impacts and their hydrodynamic transport. A sequential communication strategy is employed to reproduce the original coupled problem. This novel approach allows simulating the erosion process over macroscopic surfaces based on detailed impact simulations instead of erosion correlations.

The validation presented in this paper is very encouraging. Both the erosion distribution and the global erosion rate agree within 16% of their experimental counterparts. This level of error is an improvement over the state-of-the-art erosion simulations based on correlations [9]. Future work is focused on a wider model validation, as well as on considering the sediment shape and elasticity in the impact simulations.

ACKNOWLEDGMENTS

This work was supported by the Swiss Commission for Technology and Innovation (CTI) with grant No. 17568.1 PFEN.IW. The authors would also like to thank General Electric Power – Hydro for their financial support and technical assistance.

REFERENCES

[1] H. Grein and A. Schachenmann, "Solving problems of abrasion in hydroelectric machinery," *Water Power and Dam Construction*, pp. 19–24, 1992.

[2] C. G. Duan and V. Y. Karelin, in *Abrasive Erosion and Corrosion of Hydraulic Machinery*, ser. Series on Hydraulic Machinery. London: Imperial College Press, 2002, vol. 2.

[3] I. Finnie, "Erosion of surfaces by solid particles," *Wear*, vol. 3, pp. 87–103, 1960.

[4] G. L. Sheldon and I. Finnie, "The mechanism of material removal in the erosive cutting of brittle materials," *Journal of Engineering for Industry*, vol. 88, pp. 393–399, 1966.

[5] I. Finnie, "Some observations on the erosion of ductile materials," *Wear*, vol. 19, pp. 81–90, 1972.

[6] J. G. A. Bitter, "A study of erosion phenomena - Part I," *Wear*, vol. 6, pp. 5–21, 1963.

[7] ——, "A study of erosion phenomena - Part II," *Wear*, vol. 6, pp. 169–190, 1963.

[8] P. Shewmon and G. Sundararajan, "The erosion of metals," *Ann. Rev. Mater. Sci.*, vol. 13, pp. 301–318, 1983.

[9] G. Messa and S. Malavasi, "The effect of sub-models and parametrizations in the simulation of abrasive jet impingement tests," *Wear*, vol. 370-371, pp. 59–72, 2017.

[10] M. S. ElTobgy, E. Ng, and M. A. Elbestawi, "Finite element modeling of erosive wear," *International Journal of Machine Tools and Manufacture*, vol. 45, pp. 1337–1346, 2005.

[11] Y. F. Wang and Z. G. Yang, "Finite element model of erosive wear on ductile and brittle materials," *Wear*, vol. 265, pp. 871–878, 2008.

[12] P. Balu, F. Kong, S. Hamid, and R. Kovacevic, "Finite element modeling of solid particle erosion in AISI 4140 steel and nickel-tungsten carbide composite material produced by the laser-based power deposition process," *Tribology International*, vol. 62, pp. 18–28, 2013.

[13] Y. F. Wang and Z. G. Yang, "A coupled finite element and meshfree analysis of erosive wear," *Tribology International*, vol. 42, pp. 373–7, 2009.

[14] M. Takaffoli and M. Papini, "Material deformation and removal due to single particle impacts on ductile materials using smoothed particle hydrodynamics," *Wear*, vol. 274, pp. 50–59, 2012.

[15] X. W. Dong, G. R. Liu, Z. Li, and W. Zeng, "A smoothed particle hydrodynamics (SPH) model for simulating surface erosion by impacts of foreign particles," *Tribology International*, vol. 95, pp. 267–278, 2016.

[16] K. Sugiyama, K. Harada, and S. Hattori, "Influence of impact angle of solid particles on erosion by slurry jet," *Wear*, vol. 265, pp. 713–720, 2008.

[17] M. H. Wang, C. Huang, K. Nandakumar, P. Minev, J. Luo, and S. Chiovelli, "Computational fluid dynamics modelling and experimental study of erosion in slurry jet flows," *International Journal of Computational Fluid Dynamics*, vol. 23, pp. 155–172, 2009.

[18] H. S. Grewal, H. Singh, and E. S. Yoon, "Interplay between erodent concentration and impingement angle for erosion in dilute water-sand flows," *Wear*, vol. 332, pp. 1111–1119, 2015.

[19] C. Vessaz, E. Jahanbakhsh, and F. Avellan, in *Advances in Hydroinformatics*, ser. Springer Hydrogeology, P. Gourbesville, J. Cunge, and G. Caigneart, Eds. Springer Singapore, 2013, ch. FPM simulations of a high-speed water jet - Validation with CFD and experimental results, pp. 419–431.

[20] A. Haider and O. Levenspiel, "Drag coefficient and terminal velocity of spherical and nonspherical particles," *Powder Technology*, vol. 58, pp. 63–70, 1989.

[21] R. Mei, "An approximate expression for the shear lift force on a spherical particle at finite Reynolds number," *International Journal of Multiphase Flow*, vol. 18, pp. 145–147, 1992.

[22] *ANSYS CFX Theory Guide 14.5*. ANSYS, Inc., Canonsburg PA 15317, 2012.

[23] A. Gosman and E. Ioannides, "Aspects of computer simulation of liquid-fuelled combustors," in 19^{th} *Aerospace Sciences Meeting*. AIAA, 1981.

[24] B. J. Kohn, "Compilation of Hugoniot equations of state," Air Force Weapons Laboratory, Kirtland Air Force Base, New Mexico, Tech. Rep. AFWL-TR-69-38, 1969.

[25] J. Hallquist, *LS-DYNA Theory Manual*. Livermore Software Technology Corporation, 2006.

[26] G. R. Johnson and W. H. Cook, "Fracture characteristics of three metals subjected to various strains, strain rates, temperatures and pressures," *Engineering Fracture Mechanics*, vol. 21, pp. 31–48, 1985.

[27] J. F. Molinari and M. Ortiz, "A study of solid-particle erosion of metallic targets," *Int. J. Impact Eng.*, vol. 27, pp. 347–358, 2002.

[28] E. Jahanbakhsh, C. Vessaz, A. Maertens, and F. Avellan, "Development of a finite volume particle method for 3-D fluid flow simulations," *Comput. Methods Appl. Mech. Engrg.*, vol. 298, pp. 80–107, 2016.

[29] E. Jahanbakhsh, A. Maertens, N. Quinlan, C. Vessaz, and F. Avellan, "Exact finite volume particle method with spherical-support kernels," *Comput. Methods Appl. Mech. Engrg.*, vol. 317, pp. 101–127, 2017.

[30] M. Junk, in *Meshfree Methods for Partial Differential Equations*, ser. Lecture Notes in Computational Science and Engineering, M. Griebel and M. Schweitzer, Eds. Springer Berlin Heidelberg, 2003, vol. 26.

[31] M. Liou, "A sequel to AUSM: AUSM+," *Journal of Computational Physics*, vol. 129, pp. 364–382, 1996.

[32] H. Luo, J. Baum, and R. Löhner, "On the computation of multi-material flows using ALE formulation," *Journal of Computational Physics*, vol. 194, pp. 304–328, 2004.

[33] C. Vessaz, E. Jahanbakhsh, and F. Avellan, "Flow simulation of jet deviation by rotating pelton buckets using finite volume particle method," *Journal of Fluids Engineering*, vol. 137, p. 074501, 2015.

[34] E. Jahanbakhsh, C. Vessaz, and F. Avellan, "Silt motion simulation using finite volume particle method," *IOP Conf. Series: Earth and Environmental Science*, vol. 22, p. 052015, 2014.

[35] S. Leguizamon, E. Jahanbakhsh, A. Maertens, C. Vessaz, S. Alimirzazadeh, and F. Avellan, "Impact erosion prediction using the finite volume particle method with improved constitutive models," *IOP Conf. Series: Earth and Environmental Science*, vol. 49, p. 122010, 2016.

[36] A. Abdulle, E. Weinan, B. Engquist, and E. Vanden-Eijnden, "The heterogeoeous multiscale method," *Acta Numerica*, vol. 21, pp. 1–87, 2012.

[37] I. Kevrekidis and G. Samaey, "Equation-free multiscale computation: Algorithms and applications," *Annu. Rev. Phys. Chem.*, vol. 60, pp. 321–344, 2009.

[38] Y. Bazilevs, V. M. Calo, J. A. Cottrell, T. J. Hughes, A. Reali, and G. Scovazzi, "Variational multiscale residual-based turbulence modeling for large eddy simulations of incompressible flows," *Comput. Methods Appl. Mech. Engrg.*, vol. 197, pp. 173–201, 2007.

[39] J. H. Walther, M. Praprotnik, E. M. Kotsalis, and P. Koumoutsakos, "Multiscale simulation of water flow past a C-540 fullerene," *Journal of Computational Physics*, vol. 231, pp. 2677–2681, 2012.
[40] R. I. Saye and J. A. Sethian, "Multiscale modeling of membrane rearrangement, drainage, and rupture in evolving foams," *Science*, vol. 340, pp. 720–724, 2013.
[41] P. Koumoutsakos and J. Feigelman, "Multiscale stochastic simulations of chemical reactions with regulated scale separation," *Journal of Computational Physics*, vol. 244, pp. 290–297, 2013.
[42] W. Y. Li, J. Wang, H. Zhu, H. Li, and C. Huang, "On ultrahigh velicity micro-particle impact on steels – A single impact study," *Wear*, vol. 305, pp. 216–227, 2013.
[43] W. Y. Li, J. Wang, H. Zhu, and C. Huang, "On ultrahigh velocity micro-particle impact on steels – A multiple impact study," *Wear*, vol. 309, pp. 52–64, 2014.
[44] A. Ruiz-Angulo and M. L. Hunt, "Measurement of the coefficient of restitution for particle collissions with ductile surfaces in a liquid," *Granular Matter*, vol. 12, pp. 185–191, 2010.
[45] B. Yildirim, S. Muftu, and A. Gouldstone, "Modeling of high velocity impact of spherical particles," *Wear*, vol. 270, pp. 703–13, 2011.
[46] H. Schlichting, *Boundary Layer Theory*. McGraw-Hill, New York, 1955.